Switchable large-gap quantum spin Hall state in the two-dimensional math xmlns="http://www.w3.org/1998/Math/MathML">mi>M/mi >mrow>msub>mi mathvariant="normal">Si/mi> mn>2/mn>/msub>msub>mi>Z/mi>mn>4/mn>/msub>/m row>/math> class of materials

Rajibul Islam, Rahul Verma, Barun Ghosh, Zahir Muhammad, Arun Bansil, Carmine Autieri, and Bahadur Singh

Phys. Rev. B **106**, 245149 — Published 29 December 2022

DOI: 10.1103/PhysRevB.106.245149

Switchable large-gap quantum spin Hall state in the two-dimensional MSi_2Z_4 class of materials

Rajibul Islam,[1,2,*] Rahul Verma,[2] Barun Ghosh,[3] Zahir Muhammad,[1,4]
Arun Bansil,[3] Carmine Autieri,[1,5,†] and Bahadur Singh[2,‡]

[1] *International Research Centre MagTop, Institute of Physics, Polish Academy of Sciences, Aleja Lotników 32/46, PL-02668 Warsaw, Poland*
[2] *Department of Condensed Matter Physics and Materials Science, Tata Institute of Fundamental Research, Colaba, Mumbai 400005, India*
[3] *Department of Physics, Northeastern University, Boston, Massachusetts 02115, USA*
[4] *Hefei Innovation Research Institute, School of Microelectronics, Beihang University, Hefei 230013, P. R. China*
[5] *Consiglio Nazionale delle Ricerche CNR-SPIN, UOS Salerno, I-84084 Fisciano (Salerno), Italy*

Quantum spin Hall (QSH) insulators exhibit spin-polarized conducting edge states that are topologically protected from backscattering and offer unique opportunities for addressing fundamental science questions and device applications. Finding viable materials that host such topological states, however, remains a continuing challenge. Here, by using in-depth first-principles theoretical modeling, we predict large bandgap QSH insulators in recently synthesized bottom-up two-dimensional MSi_2Z_4 (M = Mo or W and Z = P or As) materials family with $1T'$ structure. A structural distortion in the $2H$ phase drives a band inversion between the metal (Mo/W) d and p states of P/As to realize spinless Dirac states without spin-orbit coupling. When spin-orbit coupling is included, a hybridization gap as large as $\sim$ 204 meV opens-up at the band crossing points, realizing spin-polarized conducting edge states with nearly quantized spin Hall conductivity. We also show that the inverted band gap can be tuned with a vertical electric field, which drives a topological phase transition from the QSH to a trivial insulator with Rashba-like edge states. Our study identifies 2D MSi_2Z_4 materials family in the $1T'$ structure as large bandgap, tunable QSH insulators with protected spin-polarized edge states and large spin-Hall conductivity.

I. INTRODUCTION

Following the early studies of two-dimensional (2D) materials [1–4], Kane and Mele demonstrated the existence of a quantum spin Hall (QSH) state in graphene in the presence of symmetry-allowed spin-orbit coupling (SOC) [5, 6]. The QSH state features one-dimensional (1D) conducting helical edge modes in insulating bulk due to the nontrivial winding of their electronic states [5–13]. The helical edge modes carry symmetry-protected spin-polarized electronic states that hold immense potential for designing high-efficiency quantum electronic devices with low dissipation [14–16]. The QSH state has been theoretically predicted in a variety of 2D materials and quantum well structures. However, its experimental realization has so far been demonstrated only in HgTe/CdTe and InAs/GaSb quantum wells and thin-films of $1T'-WTe_2$, $HgPt_2Se_3$, and Bi_4Br_4 at ultra-low temperatures [17–23]. A common approach to realize the QSH state is to reduce the thickness of three-dimensional (3D) Z_2 topological insulators to drive a 3D to 2D crossover and a band inversion in the surface states. This method has successfully predicted the QSH state in thin films of Z_2 topological insulators [12, 13, 24–27]. The process of fine-tuning quantum well structures or manipulating film thickness to generate an inverted hybridization gap in the surface spectrum [12, 13, 24–31], however, can modify material properties, leading to complicated electronic structures and quenching of the quantized spin Hall conductance. It is important, therefore, to look for new strategies for designing 2D materials with large inverted bandgaps in which the QSH state can survive at room temperature.

Here, we present an in-depth first-principles analysis with optimized crystal structures to demonstrate the presence of the QSH state in the recently introduced 2D materials that can be realized via a bottom-up approach without parental analogues [32–34]. These synthetic 2D materials provide a new paradigm for engineering designer states with diverse functionalities. Specifically, 2D $MoSi_2N_4$ materials were synthesized by passivating high-energy surfaces of non-layered nitrides with Si with remarkable stability under ambient conditions [34]. They show semiconducting behavior with high carrier mobility, and feature spin-valley locking, gating and thickness-tunable spin polarization, and 2D magnetism and correlation-driven quantum anomalous Hall state, among other properties depending on their compositions [35–38]. Theoretically predicted properties of these materials are reported to be superior to those of the widely used 2D transition metal dichalcogenides (TMDs) [34, 35, 39, 40]. It is not clear, however, if these materials can form polytypic structures and realize the QSH state similar to the 2D TMDs. Here, based on our molecular dynamics simulations and phonon calculations, we predict that the $1T'$ phase of MSi_2Z_4 (M = Mo or W, and Z = P or As) is stable and realizes a QSH state via a structural distortion from the 2H to $1T'$ phase. Our calculated inverted bandgap ($\sim$ 204 meV) and spin Hall

conductivity (SHC) [$\sim 1.3e^2/h$] are higher than the top-to-bottom grown 2D TMDs. We also show that the QSH state of MSi_2Z_4 can be switched off by driving a topological phase transition via an applied (vertical) electric field. Our study indicates the robust presence of a switchable QSH state in a new polytypic structure of bottom-up grown 2D materials with excellent topological and spintronics properties.

II. METHODOLOGY

Electronic structure calculations were performed within the framework of the density functional theory (DFT) based on the projector augmented wave method using the VASP [41, 42] code. The self-consistent relativistic calculations were performed with a plane wave cut-off energy of 500 eV and a Γ centered $6 \times 12 \times 1$ $k-$mesh for Brillouin zone (BZ) sampling. We used the generalized gradient approximation (GGA) to include exchange-correlation effects [43]. The structural parameters were fully optimized until the residual forces on each atom were less than 0.001 eV/Å and the total energy is converged to 10^{-8} eV. For a more accurate treatment of electronic correlations, we also employed the Heyd-Scuseria-Ernzerhof (HSE) hybrid functional with 25% exact Hartree-Fock exchange [44]. Phonon dispersions were calculated with the density functional perturbation theory (DFPT) using the PHONOPY code [45] with a 2×4×1 supercell. The *ab-initio* molecular dynamics simulations were performed through the Nose-Hoover thermostat at a constant temperature of 300 K with a time step of $2fs$ [46]. We generated material-specific tight-binding Hamiltonians with M-d, Si-s and p, and Z-p orbitals using the VASP2WANNIER interface [47], which was also used to elucidate topological properties using the Wanniertools package [48, 49].

III. RESULTS AND DISCUSSION

A. Structural properties

The pristine phase of monolayer MSi_2Z_4 belongs to the 1H crystal structure family of 2D materials with space group D^1_{3h} ($P\bar{6}m2$, No. 187) [34, 35]. Figure 1(a) shows the crystal lattice of $MoSi_2P_4$ as an exemplar system. The structure is layered along the hexagonal c axis and consists of MoP_2 layers sandwiched between two SiP layers. The Mo atoms are located at the center of the trigonal prismatic building block with six P atoms and the MoP_2 layer bonded vertically with the SiP layer [34]. In the $1T'$ phase of $MoSi_2P_4$ [Fig. 1(b)], the three atomic layers are locked in such a way that the position of Mo atoms is at the center of 60^o twisted trigonal prismatic building block with six P atoms. This creates the octahedral local coordination of Mo atoms with the six P atoms in the MoP_2 layer but with different Mo-Mo bond lengths to form zig-zag atomic chains along the y axis and period-doubling along the x axis. This structural distortion lowers the hexagonal 1H symmetry to $1T'$ monoclinic symmetry with space group $P2_1/m$ (No. 11) and forms a rectangular primitive unit cell as shown in Fig. 1(b). Importantly, the $1T'$ structure possesses the inversion symmetry I in contrast to the 1H phase. Figure 1(c) illustrates the BZs associated with both the 1H and $1T'$ phases where high-symmetry points are marked in both the pristine hexagonal and reduced rectangular BZs.

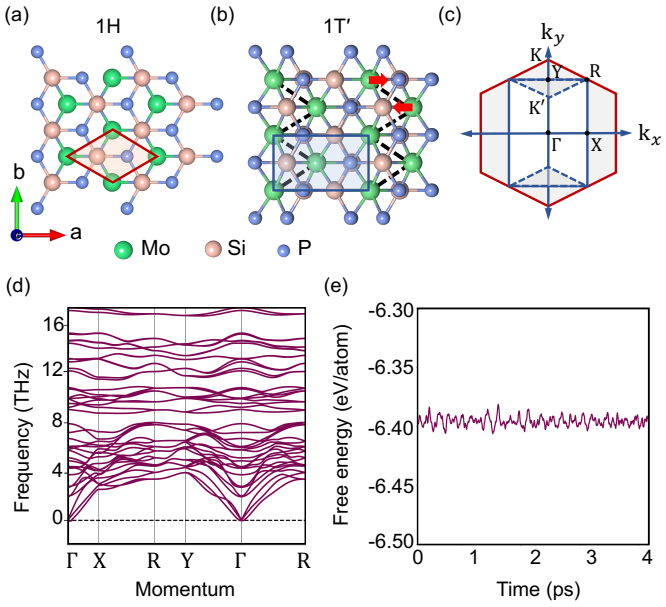

FIG. 1. Crystal structure of a $MoSi_2P_4$ monolayer in (a) 1H and (b) $1T'$ phase. The unit cell of the 1H phase is indicated by the red rhombus in (a) and that of the $1T'$ phase is shown as a blue rectangle in (b). The Mo atoms are distorted from their original hexagonal positions to form 1D zigzag chains along the y axis in the $1T'$ phase, shown with dashed-black lines in (b). (c) The associated 2D Brillouin zones (BZs) with high-symmetry points marked. The K points of the hexagonal BZ (red color) fold onto the $\Gamma - Y$ line of $1T'$ rectangular BZ (blue color). (d) Phonon dispersion in $1T'$ $MoSi_2P_4$. (e) Total free energy of monolayer $1T'$ $MoSi_2P_4$ as a function of time step during the molecular dynamics simulation at $T = 300$ K.

To determine the stability of polytypic structures, we present the calculated phonon dispersion of monolayer $1T'$ $MoSi_2P_4$ in Fig. 1(d). The absence of imaginary frequency modes throughout the BZ indicates dynamical stability of the $1T'$ phase. The structural stability is further substantiated by performing *ab-initio* molecular dynamics simulations at 300 K. Variation of the free energy as a function of the simulation time is presented in Fig. 1(e). The energy oscillates near a mean value of 6.40 eV/atom. However, the monolayer structure remains in-

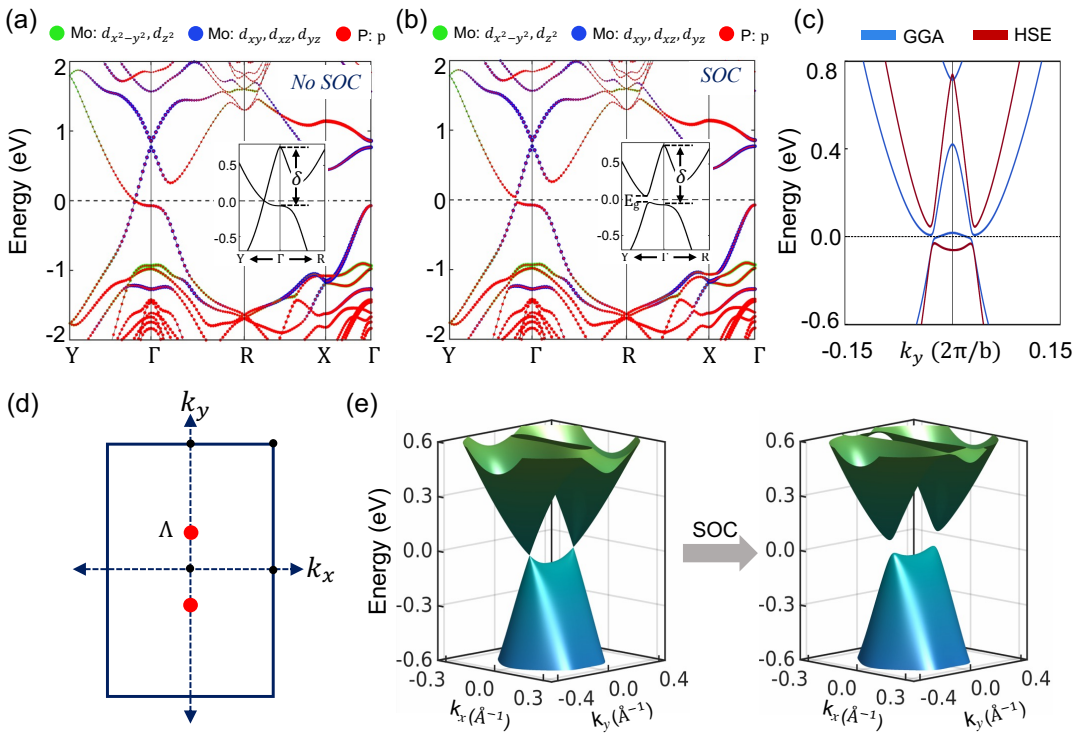

FIG. 2. Band structure of 1T′−$MoSi_2P_4$ (a) without and (b) with spin-orbit coupling using the HSE hybrid functional. The horizontal dashed line marks the Fermi level. Orbital compositions of bands are shown using different colors. Insets show closeups of bands near the Γ point at the Fermi level. Inverted bandgap (δ) and global bandgap (E_g) are marked. (c) Closeups of bands obtained with HSE and GGA functionals along the $Y-\Gamma-Y$ line. (d) Location of valence and conduction band crossings at the Fermi level without spin-orbit coupling in the 2D Brillouin zone. (e) $E-k_x-k_y$ space rendition of spin-orbit -coupling-driven electronic structure crossover in monolayer 1T′−$MoSi_2P_4$ with the HSE functional.

tact at the end of the simulations without any new reconstruction of the lattice, indicating thermal stability of the monolayer. We have also checked the thermodynamic stability of other members of the $1T'$ MSi_2Z_4 family and found them to be stable, see Supplemental Material[50]. Like the experimentally realized $1T'$ TMDs, these results indicate that the $1T'$-MSi_2Z_4 is stable and should be possible to synthesize experimentally under appropriate chemical, thermal, or mechanical conditions [51, 52]. On comparing the total energies of $1T'$, 1H, and 1T phases of MSi_2Z_4, we find that the 1H phase is the most stable, followed by the $1T'$ phase. The 1T phase is unstable and relaxes to the $1T'$ phase. The calculated energy difference between the 1H and $1T'$ phases is 55, 24, 47, and 11 meV/atom for $MoSi_2P_4$, $MoSi_2As_4$, WSi_2P_4, and WSi_2As_4, respectively. These results indicate that the $1T'$ phase can be realized under selective growth conditions as has been done, for example, for the realization of the $1T'$ phase of MoS_2 [51, 52].

B. Bulk electronic structure and band inversion

We now discuss the orbital-resolved electronic structures computed with GGA and HSE functionals to delineate the topological state of various $1T'$-MSi_2Z_4 compounds. Figures 2(a)-(b) show representative HSE band structures of $1T'$-MSi_2Z_4 taking $MoSi_2P_4$ as an example. The band structure is semimetallic with isolated spinless Dirac-type crossings on the $\Gamma-Y$ directions without SOC [Fig. 2(a)]. Adding relativistic effects opens a hybridization gap at these band crossings, thereby realizing a semiconducting state with a global bandgap, E_g^{HSE}, of 86 meV. The valence and conduction band extrema are located away from time-reversal invariant momentum (TRIM) points at $\Lambda = \pm 0.103$Å^{-1} [red dots in 2(c)] on the Γ-Y line, forming a camel-back-like band structure near the Γ point [53, 54]. Such a band structure generally points to a nontrivial topology. We find that the p states of P lie below the Mo d states with a clear band inversion at the Γ point, strong hybridization between the P and Mo states notwithstanding. This unusual orbital ordering is driven by a structural transition from 1H to $1T'$, which lowers the energy of the transition-metal states and results in a large inverted bandgap δ^{HSE} of

TABLE I. Calculated structural and electronic parameters of 2D $1T'$-MSi_2Z_4 (M = Mo or W and Z = P or As). The structural parameters include in-plane lattice constants a and b, and the interatomic separations d_1 and d_2 in the transition-metal zigzag chain. The electronic parameters presented are the global bandgap obtained with GGA (E_g^{GGA}) and HSE (E_g^{HSE}), and the inverted bandgap at the Γ point calculated with GGA (δ^{GGA}) and HSE (δ^{HSE}). Topological state is indicated: QSH denotes quantum spin Hall state. See text for details.

Material	a (Å)	b (Å)	d_1 (Å)	d_2 (Å)	Band gap (meV)		Inverted Gap (meV)		Topological invariant	Topological state
					E_g^{GGA}	E_g^{HSE}	δ^{GGA}	δ^{HSE}	Z_2	
$MoSi_2P_4$	6.141	3.430	2.945	4.194	-10.4	86.2	398	842	1	QSH
$MoSi_2As_4$	6.388	3.579	3.012	4.362	-39.5	109.2	391	800	1	QSH
WSi_2P_4	6.129	3.441	2.939	4.133	-23.2	198.5	712	1079	1	QSH
WSi_2As_4	6.364	3.589	2.993	4.368	-0.07	204.3	675	1058	1	QSH

842 meV at the Γ point that is larger than the existing $1T'$ QSH materials [The inverted bandgap δ refers to the energy gap between the highest occupied P p and the lowest unoccupied Mo d states at the Γ point, see Fig. 2]. The calculated electronic and structural parameters of our investigated $1T'$-MSi_2Z_4 materials are listed in Table I with band structures shown in the SM. Since monolayer $1T'$-MSi_2Z_4 respects inversion symmetry, we calculated the Z_2 invariant from the parity eigenvalues of the occupied states at the TRIM points and found $Z_2 = 1$ (nontrivial) in all investigated materials. We thus predict the 2D $1T'$-MSi_2Z_4 monolayers to be QSH insulators.

We present the band structures obtained using HSE06 (red curves) and GGA (blue curves) along the Y-Γ-Y directions in Fig. 2(b) to estimate the bandgap corrections in $1T'$-MSi_2Z_4 monolayers. The hybrid functionals are generally considered more accurate in estimating band bending, band order, and bandgap in comparison to the GGA. While the HSE06 is seen to correct the inverted bandgap at the Γ point in comparison to the GGA, the overall band structures obtained with the two functionals are topologically equivalent with a band inversion at the Γ point. Figure 2(d) considers the formation of the QSH state in $1T'$-MSi_2Z_4 monolayers by switching off the SOC. Specifically, the gapless band crossings are found at finite momenta along the $Y-\Gamma-Y$ line at the Λ points. Switching on the SOC, hybridizes these band crossings to generate the QSH state. These results imply that the band inversion in 2D $1T'$-MSi_2Z_4 emerges via the structural transition while the SOC is responsible for forming the QSH state.

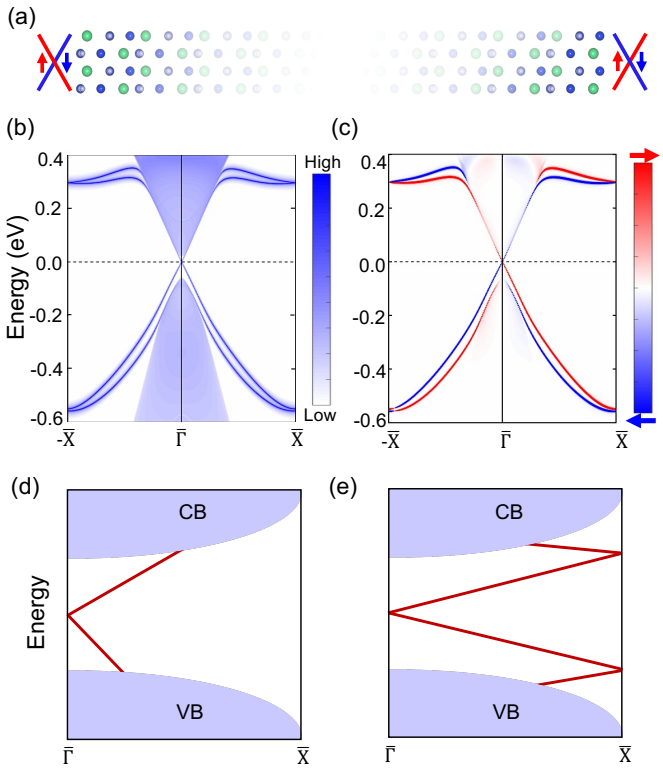

FIG. 3. (a) Lattice structure of semi-infinite one-dimensional edges of $1T'$-$MoSi_2P_4$. Spin-polarized edge states are shown schematically on the left and right edges. (b) Electronic spectrum of (010) edge. Nontrivial edge states can be seen in the 2D bulk bandgap. (c) Calculated left-edge state's spin-texture in 2D $1T'$-$MoSi_2P_4$. Red (blue) colors indicate up (down) spin polarization. (d)-(e) Schematic representations of the various nontrivial edge states (red lines) connecting the bulk valence and conduction bands (light blue color) between the two time-reversal invariant points $\overline{\Gamma}$ and $\overline{X}$.

C. Edge states and spin Hall conductivity

Appearance of spin-polarized edge states protected by the time-reversal symmetry is the hallmark of the QSH state. To highlight these states, we plot the calculated edge-state spectrum and the associated spin-texture of $MoSi_2P_4$ in Fig. 3. Figure 3(a) depicts the terminated left and right edges along the y axis with schematics of the nontrivial states of our xy monolayer (x remains the periodic direction). Since the two edges are related by inversion symmetry, we display states for the left edge in Figs. 3(b)-(c). A pair of counter-propagating states with opposite spin-polarization are seen in the bandgap with a Dirac point at $\overline{\Gamma}$. The nontrivial edge states span the whole $\overline{\Gamma}-\overline{X}$ line to connect the bulk valence and

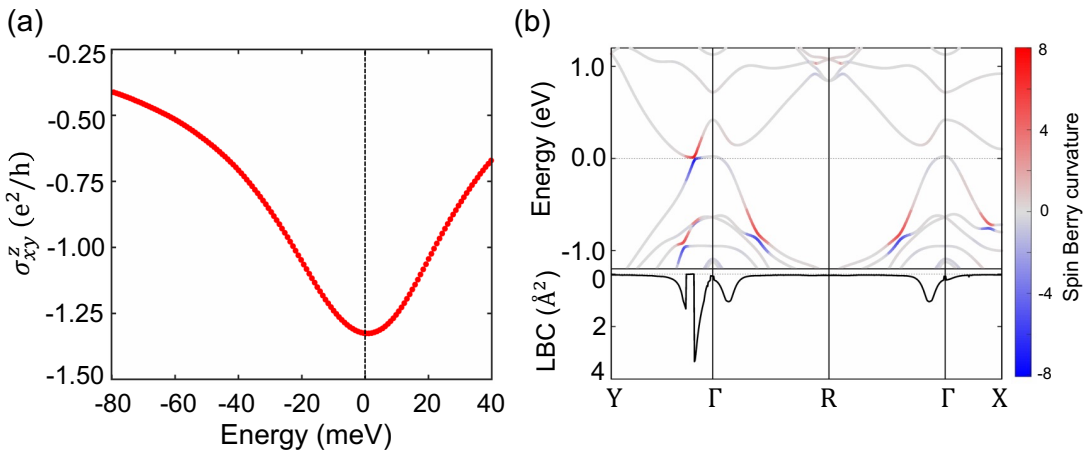

FIG. 4. (a) Intrinsic spin Hall conductivity (SHC) σ^z_{xy} as a function of Fermi energy in monolayer $1T'$-$MoSi_2P_4$. SHC is given in units of $\frac{e^2}{\hbar}$. Value of the SHC is maximum at the Fermi level. (b) Band-resolved (top) and $k-$resolved (bottom) spin Berry curvature of monolayer $MoSi_2P_4$ along the high-symmetry directions in the 2D Brillouin zone. LBC stands for logarithm of $\Omega^z_{xy}(\boldsymbol{k})$ (Eq. 2) and the colorbar refers to the logarithm of $\Omega^z_{n,xy}(\boldsymbol{k})$ (Eq. 3).

conduction bands as shown schematically in Fig. 3(e). Similar results are found for other $1T'$-MSi_2Z_4 materials.

Having established the QSH state in $1T'$-MSi_2Z_4 monolayers, we turn to discuss their intrinsic spin Hall conductivities (SHCs). We obtain the SHC σ^z_{xy} using the Kubo formula [55–59] as:

$$\sigma^z_{xy} = \frac{-e^2}{\hbar}\frac{1}{A}\sum_{k}\Omega^z_{xy}(\boldsymbol{k}) \tag{1}$$

where,

$$\Omega^z_{xy}(\boldsymbol{k}) = \sum_{n} f_n(\boldsymbol{k})\Omega^z_{n,xy}(\boldsymbol{k}) \tag{2}$$

is the k-resolved spin Berry curvature and

$$\Omega^z_{n,xy}(\boldsymbol{k}) = \hbar^2 \sum_{m\neq n} \frac{-2\mathrm{Im}\langle n\boldsymbol{k}|\hat{J}^z_x|m\boldsymbol{k}\rangle\langle m\boldsymbol{k}|\hat{v}_y|n\boldsymbol{k}\rangle}{(E_{nk}-E_{mk})^2} \tag{3}$$

is the band-resolved spin Berry curvature.

In Eqs. 1-3, A is the area of the 2D unit cell and $|n\boldsymbol{k}\rangle$ denotes the Bloch state with energy E_{nk} and occupation $f_n(\boldsymbol{k})$. The spin current operator $\hat{J}^z_x = \frac{1}{2}\{\hat{\sigma}_z, \hat{v}_x\}$ with the spin operator $\hat{\sigma}_z$ and the velocity operator $\hat{v}_x$. The SHC $\sigma^z_{x,y}$ represents the spin-current along the x direction generated by the electric field along the y direction, where the spin current is polarized along the z direction. We used a dense grid of 10^6 $k-$points in conjunction with maximally-localized Wannier functions to evaluate the spin Berry curvature and SHC. Figure 4(a) presents the calculated SHC as a function of the Fermi energy. The SHC is maximum near the band crossing points [marked with dashed line] reaching the highest value of $\sim 1.3\frac{e^2}{\hbar}$ much larger than the $1T'$ TMDs with the QSH state. Amplitude of the SHC decreases quickly away from the band crossings points. This can be further seen from our band and $k-$resolved spin Berry curvature in Fig. 4(b). The spin Berry curvature is largely concentrated near the valence and conduction band-crossing points along the $\Gamma - Y$ direction, which have a SOC-driven hybridization gap. Notably, the perfect quantization of the SHC requires an S_z-conserved Hamiltonians. However, realistic material parameters depend on the constraints of point-group symmetries, coupling of various bands, and the local atomic geometries, among other factors, which lead to nonconserved-S_z Hamiltonians [60]. As the local atomic geometry and spin-orbit interactions in MSi_2Z_4 are different from the $1T'$ TMDs, differences in their SHCs values are naturally expected [61]. An optimal setup to exploit the large SHC in $MoSi_2P_4$ would be in the clean limit with the Fermi level lying between the band crossings points.

D. Electric field switching of quantum spin Hall state

We now demonstrate the tunability of the QSH state and the switching of the topological state under a vertical electric field. Topologically inverted bands between the transition metal d and pnictogen's p orbitals lie at well-separated 2D planes in the $1T'$ monolayer. This distinct spatial location of bands provides a natural basis for their tunability via an out-of-the-plane (vertical) electric field E_z. Figure 5 shows the HSE band structure for various electric field values. The electric field induces Rashba spin-splittings in the states by breaking the inversion equivalence on the top and bottom sides of the monolayers. This is evident from spin-split states shown with distinct colors in the top row of Figs. 5(b)-(c). As the

electric field increases, the band gap decreases to zero at the critical electric field value of $E_c = 0.187$ eV/Å where the spin-up and spin-down bands cross at the opposite Λ points. With further increase in the electric field, the bandgap reopens. An analysis based on the Z_2 invariants and edge-state dispersions (Fig. 5) shows that this bandgap closing drives a change in the topology to a trivial state with $Z_2 = 0$. This topological phase transition destroys the topological edge states thereby switching off the QSH state in 1T′−$MoSi_2P_4$. A change in the polarity of the electric field shows a similar topological phase transition to a trivial state. The evolution of QSH and trivial insulator state as a function of the applied electric field is displayed in Fig. 6.

The preceding results indicate an electric field on/off control of the spin-polarized edge currents in 1T′−MSi_2Z_4 similar to the case of 1T′−TMDs [14]. Since the crystal symmetries of both these materials families are the same, various device ideas conceived for 1T'-TMDs can be applied to the MSi_2Z_4 family with the added advantage of a large, inverted bandgap and large SHC. For example, monolayer MSi_2Z_4 could be interfaced with a large bandgap 2D insulator to protect the helical edge channels from being gapped by interlayer hybridization to realize a topological transistor [14]. When the Fermi level is placed in the nontrivial bandgap, a nearly quantized SHC would be realized in this device under zero or small electric fields. An electric field beyond the critical value of ± 0.187 eV/Å can switch off the quantized spin-Hall conductance, driving it into a trivial insulating state.

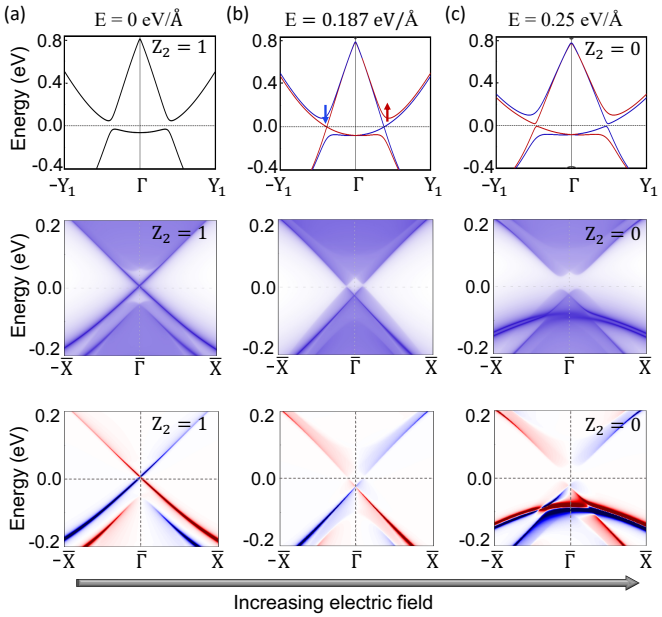

FIG. 5. Band structure of 1T′−$MoSi_2P_4$ monolayer for various values of the vertical electric field E_z: (a) 0, (b) 0.187, and (c) 0.250 eV/Å. The top, middle, and bottom rows show 2D band structure, (010) edge spectrum, and the edge-state spin-texture, respectively. Red (blue) color identifies up (down) spin state.

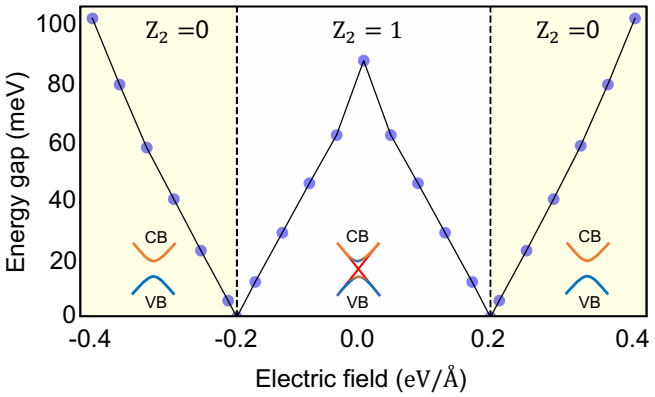

FIG. 6. Topological phase diagram of 1T′−$MoSi_2P_4$ as a function of the vertical electric field (E_z). Critical electric field strengths for the topological phase transition from $Z_2 = 1$ to $Z_2 = 0$ state is marked with vertical dashed lines.

IV. SUMMARY

We have demonstrated the existence of a tunable QSH state with a large bandgap in a new polytypic structure of the recently introduced bottom-up synthesized MSi_2Z_4 family of 2D materials. Our analysis based on phonon spectra and molecular dynamics simulations shows that these materials realize a thermodynamically stable 1T' phase in addition to the putative 1H phase. Our in-depth electronic structure modeling reveals that a structural distortion in the 1H phase leads to the 1T' structure and induces a topological band inversion. An hybridization gap as large as 204 meV is found in the MSi_2Z_4 family that is even larger than in the existing 1T′−TMDs that host a QSH ground state. Our calculated SHC shows a large value of $\sim 1.3\frac{e^2}{h}$ in $MoSi_2P_4$ that arises from the large spin Berry curvature induced by spin-orbit-split bands at the band inversion points. We also show that the QSH state is tunable with a vertical electric field, which provides an external control for switching or turning on/off the QSH state. Our study thus not only introduces a new polytypic structure of recently introduced 2D MSi_2Z_4 materials, which supports a large bandgap QSH state, but it also suggests that this materials family will potentially provide a promising new platform for realizing nontrivial states with large spin Hall conductance.

ACKNOWLEDGEMENTS

This work is supported by the Department of Atomic Energy of the Government of India under project number 12-R&D-TFR-5.10-0100. The work at Institute of Physics, Polish Academy of Sciences is supported by the Foundation for Polish Science through the International Research Agendas program co-financed by the European Union within the Smart Growth Operational Programme and the National Science Center in the framework of the "PRELUDIUM" (Decision No.: DEC-2020/37/N/ST3/02338). We acknowledge the access to the computing facilities of the Interdisciplinary Center of Modeling at the University of Warsaw, Grant G84-0, GB84-1 and GB84-7. We acknowledge the CINECA award under the ISCRA initiative IsC93 "RATIO" and IsC99 "SILENTS" grant, for the availability of high-performance computing resources and support. The work at Northeastern University was supported by the Air Force Office of Scientific Research under award number FA9550-20-1-0322 and it benefited from the computational resources of Northeastern University's Advanced Scientific Computation Center (ASCC) and the Discovery Cluster.

* rislam@magtop.ifpan.edu.pl
† autieri@magtop.ifpan.edu.pl
‡ bahadur.singh@tifr.res.in

[1] K. S. Novoselov, Nobel lecture: Graphene: Materials in the flatland, Rev. Mod. Phys. **83**, 837 (2011).
[2] A. H. Castro Neto, F. Guinea, N. M. R. Peres, K. S. Novoselov, and A. K. Geim, The electronic properties of graphene, Rev. Mod. Phys. **81**, 109 (2009).
[3] K. S. Novoselov, D. Jiang, F. Schedin, T. J. Booth, V. V. Khotkevich, S. V. Morozov, and A. K. Geim, Two-dimensional atomic crystals, Proc. Natl. Acad. Sci. **102**, 10451 (2005).
[4] S. Manzeli, D. Ovchinnikov, D. Pasquier, O. V. Yazyev, and A. Kis, 2d transition metal dichalcogenides, Nat. Rev. Mater. **2**, 17033 (2017).
[5] C. L. Kane and E. J. Mele, Phys. Rev. Lett. **95**, 226801 (2005).
[6] C. L. Kane and E. J. Mele, Phys. Rev. Lett. **95**, 146802 (2005).
[7] A. Bansil, H. Lin, and T. Das, Colloquium: Topological band theory, Rev. Mod. Phys. **88**, 021004 (2016).
[8] M. Z. Hasan and C. L. Kane, Colloquium: Topological insulators, Rev. Mod. Phys. **82**, 3045 (2010).
[9] B. Singh, H. Lin, and A. Bansil, Topology and symmetry in quantum materials, Advanced Materials , 2201058 (2022).
[10] B. A. Bernevig and S.-C. Zhang, Quantum spin hall effect, Phys. Rev. Lett. **96**, 106802 (2006).
[11] B. A. Bernevig, T. L. Hughes, and S.-C. Zhang, Science **314**, 1757 (2006).
[12] B. Singh, H. Lin, R. Prasad, and A. Bansil, Topological phase transition and two-dimensional topological insulators in ge-based thin films, Phys. Rev. B **88**, 195147 (2013).
[13] A. Marrazzo, M. Gibertini, D. Campi, N. Mounet, and N. Marzari, Prediction of a large-gap and switchable kane-mele quantum spin hall insulator, Phys. Rev. Lett. **120**, 117701 (2018).
[14] X. Qian, J. Liu, L. Fu, and J. Li, Science **346**, 1344 (2014).
[15] Y. Xu, B. Yan, H.-J. Zhang, J. Wang, G. Xu, P. Tang, W. Duan, and S.-C. Zhang, Phys. Rev. Lett. **111**, 136804 (2013).
[16] C. Liu, T. L. Hughes, X.-L. Qi, K. Wang, and S.-C. Zhang, Phys. Rev. Lett. **100**, 236601 (2008).
[17] M. KÃ¶nig, S. Wiedmann, C. BrÃŒne, A. Roth, H. Buhmann, L. W. Molenkamp, X.-L. Qi, and S.-C. Zhang, Science **318**, 766 (2007).
[18] I. Knez, R.-R. Du, and G. Sullivan, Phys. Rev. Lett. **107**, 136603 (2011).
[19] S. Tang, C. Zhang, D. Wong, Z. Pedramrazi, H.-Z. Tsai, C. Jia, B. Moritz, M. Claassen, H. Ryu, S. Kahn, *et al.*, Nat. Phys. **13**, 683 (2017).
[20] K. Kandrai, P. Vancsó, G. Kukucska, J. Koltai, G. Baranka, Á. Hoffmann, Á. Pekker, K. Kamarás, Z. E. Horváth, A. Vymazalová, L. Tapasztó, and P. Nemes-Incze, Signature of large-gap quantum spin hall state in the layered mineral jacutingaite, Nano Lett. **20**, 5207 (2020).
[21] N. Shumiya, M. S. Hossain, J.-X. Yin, Z. Wang, M. Litskevich, C. Yoon, Y. Li, Y. Yang, Y.-X. Jiang, G. Cheng, Y.-C. Lin, Q. Zhang, Z.-J. Cheng, T. A. Cochran, D. Multer, X. P. Yang, B. Casas, T.-R. Chang, T. Neupert, Z. Yuan, S. Jia, H. Lin, N. Yao, L. Balicas, F. Zhang, Y. Yao, and M. Z. Hasan, Evidence of a room-temperature quantum spin hall edge state in a higher-order topological insulator, Nat. Mater. **21**, 1111 (2022).
[22] Z. Fei, T. Palomaki, S. Wu, W. Zhao, X. Cai, B. Sun, P. Nguyen, J. Finney, X. Xu, and D. H. Cobden, Edge conduction in monolayer wte2, Nat. Phys. **13**, 677 (2017).
[23] S. Wu, V. Fatemi, Q. D. Gibson, K. Watanabe, T. Taniguchi, R. J. Cava, and P. Jarillo-Herrero, Science **359**, 76 (2018).
[24] H. Lin, R. S. Markiewicz, L. A. Wray, L. Fu, M. Z. Hasan, and A. Bansil, Single-dirac-cone topological surface states in the tlbise$_2$ class of topological semiconductors, Phys. Rev. Lett. **105**, 036404 (2010).
[25] Y.-F. Zhang, J. Pan, H. Banjade, J. Yu, H. Lin, A. Bansil, S. Du, and Q. Yan, Nano Res. **14**, 584 (2021).
[26] Z.-Y. Jia, Y.-H. Song, X.-B. Li, K. Ran, P. Lu, H.-J. Zheng, X.-Y. Zhu, Z.-Q. Shi, J. Sun, J. Wen, D. Xing, and S.-C. Li, Phys. Rev. B **96**, 041108 (2017).
[27] Z. Li, Y. Song, and S. Tang, J. Phys. Condens. Matter **32**, 333001 (2020).
[28] Y. Cao, A. Mishchenko, G. L. Yu, E. Khestanova, A. P. Rooney, E. Prestat, A. V. Kretinin, P. Blake, M. B. Shalom, C. Woods, J. Chapman, G. Balakrishnan, I. V. Grigorieva, K. S. Novoselov, B. A. Piot, M. Potemski, K. Watanabe, T. Taniguchi, S. J. Haigh, A. K. Geim, and R. V. Gorbachev, Nano Lett. **15**, 4914 (2015).
[29] L. Wang, I. Gutiérrez-Lezama, C. Barreteau, N. Ubrig, E. Giannini, and A. F. Morpurgo, Nat. Commun. **6**, 1 (2015).
[30] F. Ye, J. Lee, J. Hu, Z. Mao, J. Wei, and P. X.-L. Feng, Small **12**, 5802.

[31] J.-J. Zhang, D. Zhu, and B. I. Yakobson, Heterobilayer with ferroelectric switching of topological state, Nano Letters **21**, 785 (2021), pMID: 33356322.

[32] K. S. Novoselov, A. Mishchenko, A. Carvalho, and A. H. C. Neto, 2d materials and van der waals heterostructures, Science **353**, aac9439 (2016).

[33] K. S. Novoselov, Discovery of 2D van der Waals layered MoSi2N4 family, National Science Review **7**, 1842 (2020).

[34] Y.-L. Hong, Z. Liu, L. Wang, T. Zhou, W. Ma, C. Xu, S. Feng, L. Chen, M.-L. Chen, D.-M. Sun, *et al.*, Science **369**, 670 (2020).

[35] R. Islam, B. Ghosh, C. Autieri, S. Chowdhury, A. Bansil, A. Agarwal, and B. Singh, Phys. Rev. B **104**, L201112 (2021).

[36] C. Yang, Z. Song, X. Sun, and J. Lu, Phys. Rev. B **103**, 035308 (2021).

[37] S. Li, W. Wu, X. Feng, S. Guan, W. Feng, Y. Yao, and S. A. Yang, Phys. Rev. B **102**, 235435 (2020).

[38] X. Feng, X. Xu, Z. He, R. Peng, Y. Dai, B. Huang, and Y. Ma, Phys. Rev. B **104**, 075421 (2021).

[39] S. Bertolazzi, J. Brivio, and A. Kis, ACS nano **5**, 9703 (2011).

[40] Y. Cai, G. Zhang, and Y.-W. Zhang, J. Am. Chem. Soc **136**, 6269 (2014).

[41] P. Hohenberg and W. Kohn, Inhomogeneous electron gas, Phys. Rev. **136**, B864 (1964).

[42] G. Kresse and J. Furthmüller, Phys. Rev. B **54**, 11169 (1996).

[43] J. P. Perdew, K. Burke, and M. Ernzerhof, Phys. Rev. Lett. **77**, 3865 (1996).

[44] J. Heyd, G. E. Scuseria, and M. Ernzerhof, Hybrid functionals based on a screened coulomb potential, J. Chem. Phys. **118**, 8207 (2003).

[45] A. Togo and I. Tanaka, Scripta Materialia **108**, 1 (2015).

[46] R. N. Barnett and U. Landman, Phys. Rev. B **48**, 2081 (1993).

[47] A. A. Mostofi, J. R. Yates, Y.-S. Lee, I. Souza, D. Vanderbilt, and N. Marzari, Computer Physics Communications **178**, 685 (2008).

[48] Q. Wu, S. Zhang, H.-F. Song, M. Troyer, and A. A. Soluyanov, Computer Physics Communications **224**, 405 (2018).

[49] M. P. L. Sancho, J. M. L. Sancho, J. M. L. Sancho, and J. Rubio, Journal of Physics F: Metal Physics **15**, 851 (1985).

[50] *See Supplemental Material at [URL will be inserted here] for the stability of 1T′ MSi_2Z_4 and bulk and edge states properties of all the studied materials* (see, also, Refs. [62–66] therein).

[51] M. Calandra, Chemically exfoliated single-layer mos_2: Stability, lattice dynamics, and catalytic adsorption from first principles, Phys. Rev. B **88**, 245428 (2013).

[52] L. Liu, J. Wu, L. Wu, M. Ye, X. Liu, Q. Wang, S. Hou, P. Lu, L. Sun, J. Zheng, L. Xing, L. Gu, X. Jiang, L. Xie, and L. Jiao, Phase-selective synthesis of 1t′mos2 monolayers and heterophase bilayers, Nat. Mater. **17**, 1108 (2018).

[53] R. Islam, B. Ghosh, G. Cuono, A. Lau, W. Brzezicki, A. Bansil, A. Agarwal, B. Singh, T. Dietl, and C. Autieri, Topological states in superlattices of hgte class of materials for engineering three-dimensional flat bands, Phys. Rev. Research **4**, 023114 (2022).

[54] G. Hussain, A. Samad, M. Ur Rehman, G. Cuono, and C. Autieri, Emergence of rashba splitting and spin-valley properties in janus mogesip2as2 and wgesip2as2 monolayers, Journal of Magnetism and Magnetic Materials **563**, 169897 (2022).

[55] L. Matthes, S. Küfner, J. Furthmüller, and F. Bechstedt, Intrinsic spin hall conductivity in one-, two-, and three-dimensional trivial and topological systems, Phys. Rev. B **94**, 085410 (2016).

[56] Y. Sun, Y. Zhang, C. Felser, and B. Yan, Strong intrinsic spin hall effect in the taas family of weyl semimetals, Phys. Rev. Lett. **117**, 146403 (2016).

[57] R. Zhang, C.-Y. Huang, J. Kidd, R. S. Markiewicz, H. Lin, A. Bansil, B. Singh, and J. Sun, Weyl semimetal in the rare-earth hexaboride family supporting a pseudonodal surface and a giant anomalous hall effect, Phys. Rev. B **105**, 165140 (2022).

[58] J. Zhou, J. Qiao, A. Bournel, and W. Zhao, Intrinsic spin hall conductivity of the semimetals $mote_2$ and wte_2, Phys. Rev. B **99**, 060408 (2019).

[59] J. Qiao, J. Zhou, Z. Yuan, and W. Zhao, Calculation of intrinsic spin hall conductivity by wannier interpolation, Phys. Rev. B **98**, 214402 (2018).

[60] F. Matusalem, M. Marques, L. K. Teles, L. Matthes, J. Furthmüller, and F. Bechstedt, Quantization of spin hall conductivity in two-dimensional topological insulators versus symmetry and spin-orbit interaction, Phys. Rev. B **100**, 245430 (2019).

[61] Understanding the mechanisms responsible for large SHCs in MSi_2Z_4 compared to TMDs would be interesting, but it requires an in-depth comparison of their geometric and electronic properties, which is considered outside the scope of this study.

[62] A. A. Soluyanov and D. Vanderbilt, Computing topological invariants without inversion symmetry, Phys. Rev. B **83**, 235401 (2011).

[63] A. Alexandradinata, X. Dai, and B. A. Bernevig, Wilson-loop characterization of inversion-symmetric topological insulators, Phys. Rev. B **89**, 155114 (2014).

[64] R. Yu, X. L. Qi, A. Bernevig, Z. Fang, and X. Dai, Equivalent expression of F_2 topological invariant for band insulators using the non-abelian berry connection, Phys. Rev. B **84**, 075119 (2011).

[65] A. Bouhon and A. M. Black-Schaffer, Global band topology of simple and double dirac-point semimetals, Phys. Rev. B **95**, 241101 (2017).

[66] C. Autieri, A. Bouhon, and B. Sanyal, Gap opening and large spin-orbit splitting in (m = mo,w; x = s, se, te) from the interplay between crystal field and hybridisations: insights from ab-initio theory, Philosophical Magazine **97**, 3381 (2017).